applied sciences

Article

Enhancing Safety in Automatic Electric Vehicle Charging: A Novel Collision Classification Approach

Haoyu Lin, Pengkun Quan, Zhuo Liang, Dongbo Wei and Shichun Di *

School of Mechatronics Engineering, Harbin Institute of Technology, Harbin 150001, China; linhaoyu@hit.edu.cn (H.L.); quanpengkun@hit.edu.cn (P.Q.); liangzhuo@hit.edu.cn (Z.L.); weidb@hit.edu.cn (D.W.)
* Correspondence: dishichun@hit.edu.cn; Tel.: +86-139-046-05946

Abstract: With the rise of electric vehicles, autonomous driving, and valet parking technologies, considerable research has been dedicated to automatic charging solutions. While the current focus lies on charging robot design and the visual positioning of charging ports, a notable gap exists in addressing safety aspects during the charging plug-in process. This study aims to bridge this gap by proposing a collision classification scheme for robot manipulators in automatic electric vehicle charging scenarios. In situations with minimal visual positioning deviation, robots employ impedance control for effective insertion. Significant deviations may lead to potential collisions with other vehicle parts, demanding discrimination through a global visual system. For moderate deviations, where a robot's end-effector encounters difficulty in insertion, existing methods prove inadequate. To address this, we propose a novel data-driven collision classification method, utilizing vibration signals generated during collisions, integrating the robust light gradient boosting machine (LightGBM) algorithm. This approach effectively discerns the acceptability of collision contacts in scenarios involving moderate deviations. Considering the impact of passing vehicles introducing environmental noise, a noise suppression module is introduced into the proposed collision classification method, leveraging empirical mode decomposition (EMD) to enhance its robustness in noisy charging scenarios. This study significantly contributes to the safety of automatic charging processes, offering a practical and applicable collision classification solution tailored to diverse noisy scenarios and potential contact forms encountered by charging robots. The experimental results affirm the effectiveness of the collision classification method, integrating LightGBM and EMD, and highlight its promising prediction accuracy. These findings offer valuable perspectives to steer future research endeavors in the domain of autonomous charging systems.

Keywords: collision classification; plug-in safety; automatic charging; light gradient boosting machine; empirical mode decomposition

Citation: Lin, H.; Quan, P.; Liang, Z.; Wei, D.; Di, S. Enhancing Safety in Automatic Electric Vehicle Charging: A Novel Collision Classification Approach. *Appl. Sci.* **2024**, *14*, 1605. https://doi.org/10.3390/app14041605

Academic Editors: Giovanni Boschetti, Matteo Bottin and Riccardo Minto

Received: 15 January 2024
Revised: 7 February 2024
Accepted: 9 February 2024
Published: 17 February 2024

1. Introduction

With the proliferation of electric vehicles, the maturation of autonomous driving, and the development of valet parking technologies, extensive research has been conducted on automatic charging solutions for electric vehicles. In the rapidly advancing field of artificial intelligence, the utilization of robots for the automatic charging of electric vehicles is regarded as an ideal solution. Currently, research in the domain of automatic electric vehicle charging primarily focuses on the design of charging robots [1,2] and the visual positioning of charging ports [3–7]. However, a notable gap remains in the research concerning the safety aspects of robots during the charging plug-in process. When addressing the safety of the automatic charging plug-in process, collisions involving robots become an inevitable challenge. Despite the generally reliable precision of visual systems in providing accurate charging port localization, external environmental factors, such as extreme lighting conditions, temperature variations, and humidity, can lead to visual positioning failures.

In such situations, the absence of an effective collision protection system poses a risk of damage to the robot and the vehicle.

Currently, research on the issue of robot collisions is primarily concentrated in the field of physical human–robot interaction (pHRI) [8]. In this field, robots are often employed in unstructured and highly dynamic environments, where contact or collisions with humans are sometimes unavoidable. Due to the diverse forms and processes of collision contact, there is currently no one-size-fits-all approach to handling such situations. In [9], an insightful collision processing pipeline is proposed, breaking down the core processes of collision into collision detection [10,11], collision localization [12,13], collision identification [8,14], collision classification [15,16], and reaction after collision [17,18]. Among these, collision classification holds significant importance in ensuring human–robot safety. Its purpose is to predict the severity of the potential damage caused by a collision or the acceptability of the collision contact. This step serves as a direct decision-making point for the robot to respond appropriately in the event of a collision. Effective collision classification methods can substantially enhance the safety of robot systems.

Although the objectives of the collision processing stages mentioned above differ, there is a certain degree of commonality in the methods employed across these processing stages. These methods are primarily categorized into model-based collision processing methods, tactile-sensor-based collision processing methods, and data-driven collision processing methods [15]. Model-based collision processing methods offer the advantage of efficiently utilizing onboard sensors to address collision issues without the need for external sensor intervention, thereby significantly reducing the cost of collision issue resolution [10,17]. However, their effectiveness in addressing collision problems is constrained by differences between the constructed observation model and the actual physical characteristics, resulting in limited precision in problem resolution. In contrast, the use of tactile sensors often provides a precision advantage in handling collision problems [19,20]. These sensors are typically deployed in the form of artificial skin on robots, enabling more refined collision processing. However, the manufacturing process for such artificial skin is often complex, and these sensors may not be suitable for scenarios involving high loads and frequent contact due to their direct interaction with the target being manipulated or protected. With the advancement of artificial intelligence technology, supervised learning-based methods are increasingly being introduced when addressing collision problems [8,21]. These methods, collectively referred to as data-driven collision processing methods, can be implemented using both onboard and external sensors. By combining reasonable data acquisition rules, the level of precision when addressing collision problems can rival that of tactile-sensor-based collision processing methods.

Regarding the extremely open issue of collision classification, it is often necessary to integrate the practical application scenarios of robots, potential contact forms, and other factors to design a rational collision classification strategy. This is crucial for significantly enhancing the applicability of the proposed classification methods in their corresponding domains. In the context of robot-based automatic electric vehicle charging, when there is minimal deviation in visual positioning, a robot can achieve effective insertion through impedance control. When there is a significant deviation in visual positioning, it may result in the end effector of the robot not making contact with the charging port but instead coming into contact with other parts of the electric vehicle. Due to the evident disparity, deploying a global visual system in the world coordinate system can facilitate collision contact discrimination, thereby preventing potential damage. When there is a moderate deviation in visual positioning and the end effector of the robot, carrying the charger is still able to make contact with the charging port but encounters difficulty in insertion, so the aforementioned methods are unable to address this situation. Given the limited size of the collision area and the frequent insertions, often involving significant insertion force, the system faces potential safety risks when lacking the capability to classify collisions in such scenarios. In order to enhance the system's safety, this paper proposes a novel data-driven collision classification method. Utilizing the vibration signals generated during collisions, the objective is to effectively discern whether the collision contact is acceptable in scenarios involving moderate deviations. Additionally, given the presence of passing vehicles introducing environmental noise in the automatic charging scenario, this paper also specifically introduces a noise suppression module into the proposed collision classification method to enhance the robustness of the proposed method in noisy scenarios.

The rest of this paper is organized as follows: Section 2 reviews related work and clarifies the main contributions of this article. Section 3 describes the details of the datasets and the framework of the proposed method. Section 4 presents and discusses the experimental results, and Section 5 concludes this paper.

2. Related Work

Generally, vibration-signal-based collision processing for robots, acknowledged as an engineering-oriented challenge, is essentially the task of classifying time-series signals that exhibit distinctions arising from collisions. Commonly employed methods for processing time-series signals include support vector machine (SVM), k-nearest neighbor (KNN), and artificial neural network (ANN). Min et al. [14] proposed a collision detection and identification approach for robots, utilizing frequency domain features derived from vibration information coupled with an ANN. This method not only effectively detects collisions but also identifies the specific link where a collision occurred. McMahan et al. [21] achieved high-precision collision localization on a single link of a robot by leveraging an SVM in conjunction with a rational strategy for collecting collision vibration information. In addition to utilizing vibration signals to construct collision processing models, there are also methods that leverage joint torque information to address collision-related issues. Zhang et al. [8] utilized joint torque signals in conjunction with KNN, SVM, and feed-forward neural network (FNN) methods to classify collisions occurring between robots and humans. This approach effectively distinguishes between intentional contact and accidental collisions involving a specific link of a robot. Additionally, some supervised learning methods based on manual feature extraction in tasks such as robot fault detection and fault-tolerant control, as mentioned in [22,23], are also worth considering for reference.

With the advancement of deep learning technologies, the convolutional neural network (CNN) [24] and recurrent neural network (RNN) [25] have been widely applied for the classification of time-series signals. Abhishek Iyer et al. [26] designed a hybrid model combining a CNN and long short-term memory (LSTM) for human emotion analysis based on electroencephalogram (EEG) data. This model successfully classifies human emotions into neutral, positive, and negative categories. Arun Prasath G et al. [27] integrated an RNN and a CNN to develop a speech recognition method to assist individuals with hearing impairments in translating spoken language into sign language. Anas H. Aljemely et al. [28] constructed an efficient bearing fault diagnosis architecture by employing LSTM with a large-margin nearest neighbor algorithm. Yiyao An et al. [29] successfully implemented the diagnosis of non-uniform bearing vibration signals in the presence of disturbances by introducing attention mechanisms into LSTM. In our previous research, we attempted to explore the possibility of simultaneous collision localization and collision classification at the end effector of a manipulator by fusing a CNN with an SVM [15]. However, in practical applications, complex deep learning models often demand significant computational resources, requiring high-end GPUs or dedicated hardware for efficient training and deployment. This significantly increases equipment costs.

This study makes a significant contribution by proposing a refined collision classification method based on the light gradient boosting machine (LightGBM) that exhibits reduced dependence on GPUs. In order to enhance the robustness of the proposed method against noise interference, we introduce a noise suppression technique based on empirical mode decomposition (EMD) as a preprocessing step for LightGBM training. This strategic approach to collision classification aims to maintain model performance while lowering computational costs, offering a more economically efficient solution for deploying collision classification systems in resource-constrained environments. Simultaneously, this work fills the gap in the related research on collision processing for the automatic charging of electric vehicles in noisy scenarios.

3. Materials and Methods

3.1. Dataset Construction

To validate the effectiveness of the proposed method, we designed an experimental setup, as illustrated in Figure 1. The experimental setup primarily consisted of a charging robot based on an Aubo-i5 and a test platform. The charger was connected to the charging robot through a flexible wrist, and an Inertial Measurement Unit (IMU) was mounted above the charger to capture vibration data during collisions with the charging port. The vibration signal comprised three-axis acceleration and three-axis angular velocity. The test platform was capable of vertical movement and yaw adjustment, providing different poses for the charging port in space.

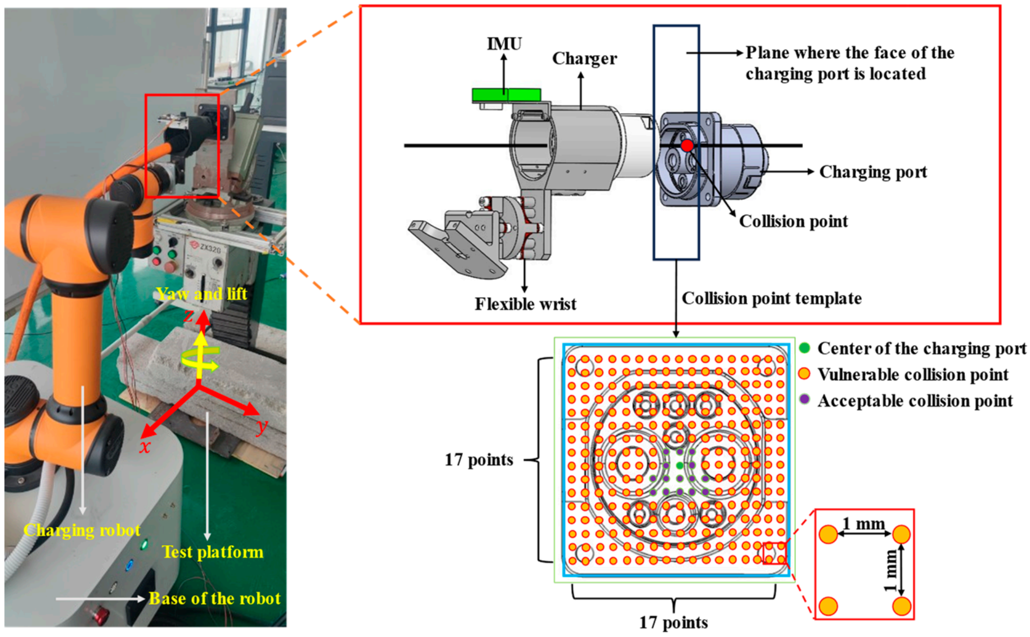

Figure 1. Illustration of experimental setup and collision domain.

To obtain reasonable data related to collisions between the charger and the charging port, it was necessary to describe the data acquisition method. In line with the actual application scenario, the robot connected the charger and the charging port in a linear motion, as shown in Figure 2. The linear motion speed at the end effector of the robot was set to 15 mm/s, and the IMU had a sampling frequency of 1500 Hz. Regarding the relative position during a collision between the charger and the charging port, we adopted the approach described in [15]. Specifically, we defined the intersection of the center axis of the charger and the plane where the end face of the charging port was located as the collision point. Based on this description, we designed a collision point template, consisting of 289 points in total, arranged in a grid of 17 rows and 17 columns, with adjacent points spaced 1 mm apart. This collision point template effectively captured situations where there was incomplete alignment and deviation between the charger and the charging port during the plug-in process. In the plug-in process, due to the presence of a flexible wrist, when the deviation was within a certain range, even if there was a collision between the charger and the charging port, the charger could still be inserted into the charging port. We defined the collision points in such situations as acceptable collision points. When the deviation exceeded a certain range and the collision prevented the charger from being inserted, or if insertion would have caused significant deformation in the flexible wrist, leading to potential plastic deformation, we defined the collision points as vulnerable collision points.

In this study, impedance control strategies were not considered during the experiments. We solely focused on the scenario where the robot connected the charger to the charging port in a linear motion. Theoretically, the introduction of impedance control could enlarge the acceptable domain, but this aspect is beyond the scope of this paper's discussion. It is worth noting that due to the non-coaxial alignment between the charger and the flexible wrist, when the charger came into contact with the charging port, it induced a counterclockwise rotation along the y-axis. Therefore, the acceptable domain in the experiment exhibited asymmetry relative to the horizontal centerline of the charging port. Specifically, it was composed of 15 acceptable collision points and 1 center collision point from the collision point template. The region formed by the remaining collision points in the template was defined as the vulnerable domain. The primary objective of this study was to predict whether collisions occurred in the acceptable domain or the vulnerable domain.

Figure 2. Illustration of the charging plug-in process.

As mentioned in [14,15,30], theoretically, variations in joint configurations at the moment of impact may impact the collision processing methods based on vibration signals. In the data collection process in this study, data were also collected at different joint configurations at the moment of collision. Given that the joint configurations at the moment of collision differed for each collision point within the collision point template with the same spatial pose, in order to create clear distinctions, we collected data on the collision point template at different heights and different relative angular deviations between the charger and the charging port to represent the different joint configurations of the robot. The specific parameters are shown in Table 1. Here, the term 'height' refers to the relative height of the charging port compared to the robot base. Initially, data collection was conducted without any angular deviation between the charger and the charging port. We established a collision point template at intervals of 20 mm, collecting collision vibration data for each collision point within the template. To ensure the reliability of the data for a single collision point, five collision experiments were conducted under the same conditions, resulting in 1445 samples for a collision point template at a single height. Additionally, to enhance the generalization ability and stability of the trained model, collision samples from every set of three adjacent heights were aggregated to create a dataset. This process resulted in three distinct datasets, identified as C1, C2, and C3, each comprising 4335 samples. Furthermore, we considered cases where there was an angular deviation between the charger and the charging port. Due to limitations in the yaw angle precision of the experimental platform, experiments were conducted with angular deviations of 1°, 2°, and 3° based on the height of C1. The corresponding datasets were labeled as C4, C5, and C6, with each dataset containing the same number of samples as C1. Furthermore, to simulate the presence of noise, we introduced varying intensities of noise on the basis of C1–C6. The intensity of the noise was defined using the Signal-to-Noise Ratio (SNR). Specifically, we introduced additive Gaussian noise with SNR values of $-9, -7, \ldots, 9$.

Table 1. Distribution of the datasets.

Dataset	Angular Deviation (°)	Number of Samples	Height (mm)
C1	0	4335	1047 1027 1007
C2	0	4335	987 967 947
C3	0	4335	927 907 887
C4	1	4335	1047 1027 1007
C5	2	4335	1047 1027 1007
C6	3	4335	1047 1027 1007

3.2. LightGBM Model Concept

LightGBM (light gradient boosting machine) is a gradient boosting framework designed to handle large-scale datasets efficiently. It is a type of gradient boosting decision tree (GBDT) algorithm that was introduced by Ke et al. in 2017 [31]. The primary objective of LightGBM is to overcome the computational challenges associated with traditional GBDT algorithms, especially when dealing with massive amounts of data. The effectiveness of LightGBM stems from the incorporation of two key techniques based on GBDT: gradient-based one-side sampling (GOSS) and exclusive feature bundling (EFB). GOSS is a sampling technique that selectively targets the most informative samples for each tree, enhancing computational efficiency while maintaining high accuracy. EFB, on the other hand, focuses on bundling features with similar distributions into a single feature, reducing the overall number of features that require processing.

More specifically, given the supervised training set $X = \{(x_i, y_i)\}_{i=1}^{n}$, where x_i represents the input features, y_i is the corresponding label, and n is the number of instances, LightGBM seeks to determine the approximation $\widetilde{h}(x)$ of the target function $h^*(x)$. The goal is to minimize the expected value of the predefined loss function $L\left(y, \widetilde{h}(x)\right)$.

Then, a number of K regression trees ($\sum_{k=1}^{K} h_k(X)$) are integrated into LightGBM to approximate the final model, which is expressed as follows:

$$h_K(X) = \sum_{k=1}^{K} h_k(X), \quad (1)$$

In LightGBM, the objective function is efficiently approximated using Newton's method. Therefore, the training process of LightGBM can be expressed in the following additive form:

$$F_k \cong \sum_{i=1}^{n} (p_i h_k(x_i) + \frac{1}{2} q_i h_k^2(x_i)), \quad (2)$$

where p_i and q_i denote the first-order and second-order gradient statistics of the loss function. Additionally, the regression tree is represented as $t_{r(x)}$, $r \in \{1, 2, \ldots, J\}$, where J denotes the number of leaves, r stands for the decision rules of the tree, and t represents a vector that denotes the sample weight of the leaf nodes. Moreover, I_j denotes the sample set of leaf j. Equation (2) can be transformed as follows:

$$F_k = \sum_{j=1}^{J} \left(\left(\sum_{i \in I_j} p_i \right) t_j + \frac{1}{2} \left(\left(\sum_{i \in I_j} q_i + \gamma \right) t_j^2 \right) \right), \tag{3}$$

where γ represents the hyperparameters. Further employing the optimization method outlined in [32], we obtain the following final optimized function:

$$O = \frac{1}{2} \left(\frac{\left(\sum_{i \in I_L} p_i\right)^2}{\sum_{i \in I_L} q_i + \gamma} + \frac{\left(\sum_{i \in I_R} p_i\right)^2}{\sum_{i \in I_R} q_i + \gamma} - \frac{\left(\sum_{i \in I} p_i\right)^2}{\sum_{i \in I} q_i + \gamma} \right), \tag{4}$$

where I_L and I_R represent the sample sets for the left and right branches, respectively. As discussed in [32], unlike traditional GBDT-based techniques, LightGBM grows trees vertically. This unique approach makes LightGBM an effective method for processing large-scale data and features. For a more detailed introduction to LightGBM, please refer to [31] by Ke et al.

3.3. EMD Concept

Empirical mode decomposition (EMD) is a signal processing technique that assumes a signal, $y(t)$, can be decomposed into independent oscillation modes known as intrinsic mode functions (IMFs). IMFs are characterized by certain conditions to ensure meaningful instantaneous physical frequencies. Specifically, each IMF must satisfy the following two conditions [33]:

1. The counts of zero crossings and extreme points should either be equal or differ by, at most, one across the entire data range;
2. At each data point, the average value of the upper envelope and the lower envelope of the local data should be zero.

The EMD method decomposes a multicomponent signal into a series of IMFs arranged from high to low frequencies, along with a trend item. Each IMF is a signal that satisfies the physical interpretation of a single oscillation mode and a single component signal. Huang proposed a sifting process for EMD, where each round of sifting separates one IMF. The process involves subtracting the obtained IMF from the original signal and repeating the sifting process until termination criteria are met. The specific decomposition process is as follows:

$$\widetilde{x}(t) = x(t) + n(t), \tag{5}$$

where $x(t)$ represents the noise-free signal and $n(t)$ represents the additive noise in the signal. Third-order spline curve fitting is employed for both the lower envelope ($e_l(t)$) and upper envelope ($e_u(t)$), ensuring that the signal remains bounded between these two envelopes. Subsequently, the mean curve ($m_1(t)$) for the maxima and minima envelopes is obtained as follows:

$$m_1(t) = \frac{e_l(t) + e_u(t)}{2}, \tag{6}$$

Then, the difference between the signal to be decomposed and the mean curve can be defined as follows:

$$h_1(t) = \widetilde{x}(t) - m_1(t), \tag{7}$$

At this point, it is necessary to determine whether $h_1(t)$ satisfies the conditions for being a valid IMF. If $h_1(t)$ meets the criteria for being an IMF, it is defined as a first-order IMF component ($c_1(t)$). If it does not meet the conditions for being an IMF, $h_1(t)$ is considered as the signal to be further decomposed, and the process outlined in Equations (6) and (7) is repeated until the resulting signal satisfies the IMF conditions. This newly obtained signal is then defined as the first-order IMF component $c_1(t)$. Subsequently, based on this, the residual signal, stripped of the IMF component, can be represented as

$$r_1(t) = \widetilde{x}(t) - c_1(t), \tag{8}$$

Then, using the residual signal as the new signal to be decomposed, the process from Equations (5)–(8) is repeated until the resulting signal after the mth decomposition cycle, denoted as $r_m(t)$, becomes a monotonic function or a constant. In the context of EMD, at this point, the initial noisy collision vibration signal can be represented as

$$\widetilde{x}(t) = \sum_{i=1}^{m} c_i(t) + r_m(t) \tag{9}$$

3.4. Workflow of the Proposed Method

The workflow of the proposed EMD-LightGBM collision classification method is illustrated in Figure 3. Initially, the data resource comprised collision vibration data acquired through the insertion and collision of each point on the collision point template. Subsequently, normalization was applied to the six-axis vibration signals to eliminate scale differences between the vibration features across different axes. The typical six-axis collision vibration signals and their corresponding normalized forms are shown in Figure 4. Here, we adopted the term 'effective period', as introduced in [15], to describe the actual length of the training data. Additionally, in consideration of signal variations during the collision, the effective period encompassed the length of the time series preceding the collision. For ease of comparison and analysis, this work standardized the length of the time series preceding the collision for vibration signals at different collision points to 50 sampling points. Following preprocessing, the data were partitioned into training and testing sets. To ensure there was no leakage of information from the testing set to the training set, distinct joint configurations were employed during the acquisition of the testing set, which were entirely different from those used to obtain the training set in this study. To enhance model performance while reducing computational complexity, feature selection was essential. In this work, we initially used the ReliefF [34] method to rank the importance of predefined features. Subsequently, redundant features were eliminated using LightGBM, KNN, SVM, and FNN methods. The use of these four methods was primarily for fairness in model validation and comparison. During the model validation and comparison stage, the comparative methods mentioned in [8], KNN, SVM, and FNN, were employed. In practical applications, it is suggested to consider using LightGBM independently to remove redundant features. It is worth noting that our feature selection process involved signals without introducing noise. After identifying suitable features, signals with noise underwent EMD. This was followed by a denoising reconstruction process to generate new vibration signals. The resulting vibration signals then underwent feature extraction based on the chosen feature representation. Following this, the LightGBM model was trained using the extracted features. In addition, during testing, the same EMD and reconstruction process for signals containing noise applied in the training process was used on the test data. The identical feature representation method was directly applied to the reconstructed signals of the testing set for feature extraction. The extracted features were then utilized to evaluate the trained model.

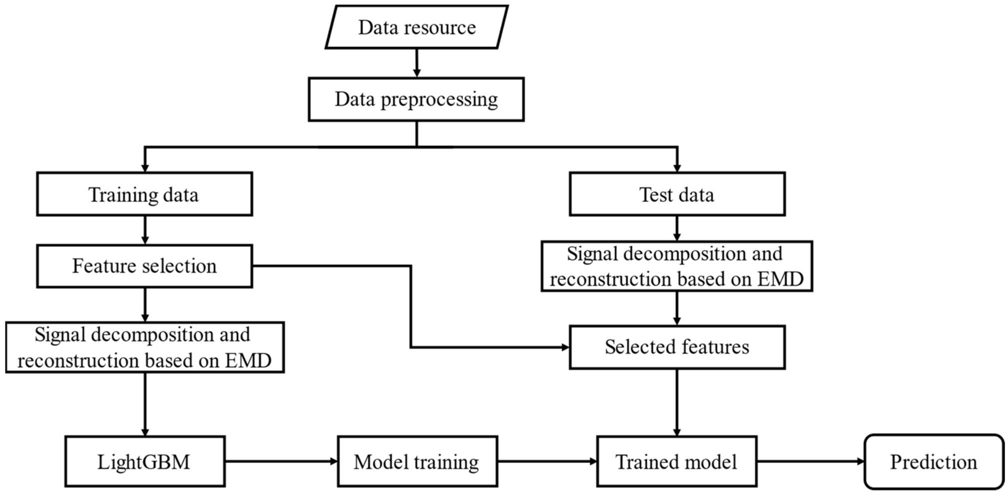

Figure 3. Workflow of the proposed collision classification method.

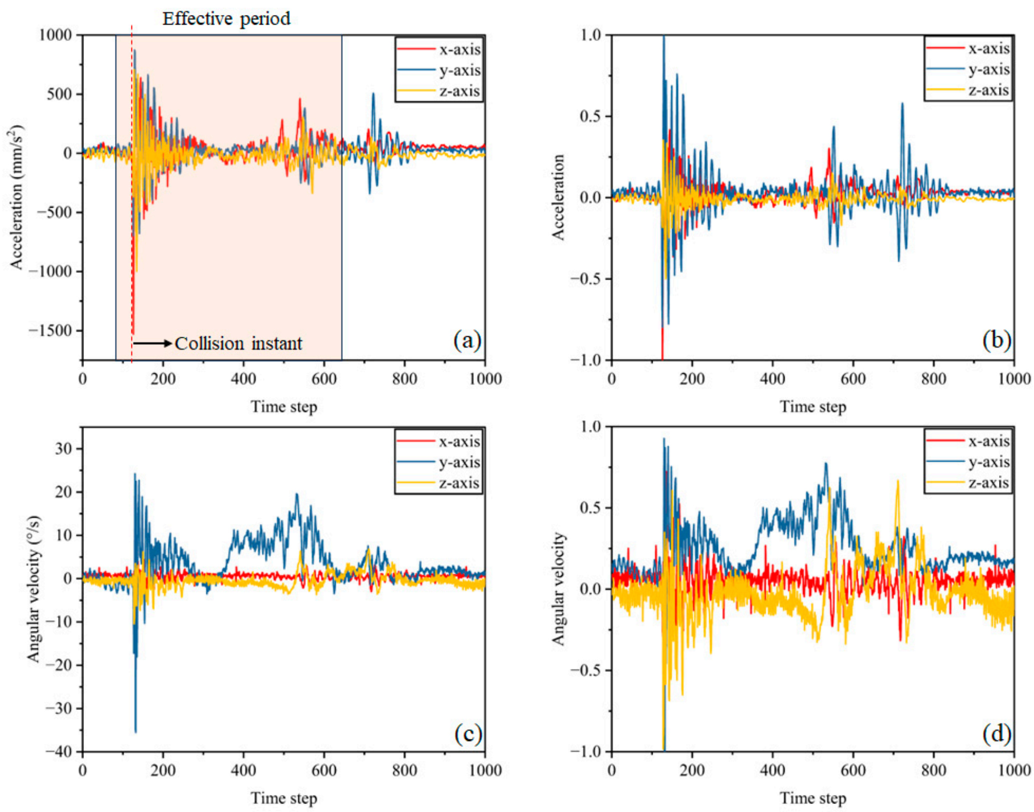

Figure 4. Waveform of a typical collision vibration signal. (**a**) Raw acceleration. (**b**) Normalized acceleration. (**c**) Raw angular velocity. (**d**) Normalized angular velocity.

4. Experimental Results and Discussion

4.1. Feature Selection Results

This section emphasizes effective feature selection using the predefined feature representation outlined in Table 2, which is an extension of the work presented in [8]. The identifiers 'T' and 'F' are used to denote time domain features and frequency domain features, respectively. To ensure optimal model performance during feature selection, the initial step involved the critical task of hyperparameter optimization for various models utilizing predefined features. In this context, we set the effective period length to 800 sample points, and the chosen optimization method was the Grid Search approach [35]. A Grid Search systematically explores a predefined hyperparameter space through exhaustive attempts of different parameter combinations to identify the optimal combination on the validation set. To capture comprehensive feature information, the incorporation of a sliding window is imperative. However, the selection of an appropriate sliding window size is pivotal. A window that is too small may risk losing medium-scale features, influenced by transient information, leading to an increased number of extracted features and, subsequently, elevated data feature redundancy, thereby reducing computational efficiency. Conversely, an excessively large window size induces significant overlap, resulting in information redundancy and a reduction in independence between features. Moreover, an overly large size may average or blur specific feature variations, causing distortion. We determined the sliding window length to be 20% of the effective period's length, with a 50% overlap between adjacent sliding windows. Additionally, to avoid the leakage of testing information during the feature selection process, we solely utilized the C1 dataset to optimize model parameters. The optimization results for the hyperparameters of different models are presented in Table 3.

Table 2. Predefined feature representations.

Feature Type Identifier	Name of Feature	Feature Definition
T1	Mean	$M = \frac{1}{n}\sum_{i=1}^{n}\tau_i$
T2	Median	$M_d = \begin{cases} \tau_{(n+1)/2}, & n \textit{ is odd} \\ \frac{\tau_{n/2} + \tau_{(n/2)+1}}{2}, & n \textit{ is even} \end{cases}$
T3	Root mean square	$RMS = \sqrt{\frac{1}{n}\sum_{i=1}^{n}{\tau_i}^2}$
T4	Variance	$V = \frac{1}{n}\sum_{i=1}^{n}(\tau_i - M)^2$
T5	Standard deviation	$SD = \sqrt{V}$
T6	Skewness	$SK = \frac{1}{n}V^{-(3/2)}\sum_{i=1}^{n}(\tau_i - M)^3$
T7	Kurtosis	$K = \frac{1}{n}V^{-2}\sum_{i=1}^{n}(\tau_i - M)^4 - 3$
T8	Coefficient of variation	$CV = \frac{SD}{M}$
T9	Extreme range	$ER = \max(\lvert\tau_i\rvert) - \min(\lvert\tau_i\rvert)$
T10	Extreme deviation	$ED = \max(\lvert\tau_i\rvert) - M$
T11	Energy increasing rate	$EIR = \frac{1}{2}\lg(\frac{\sum_{i=n/2}^{n}{\tau_i}^2}{\sum_{i=1}^{n/2}{\tau_i}^2})$
F1	Mean frequency	$\overline{f}$
F2	Fundamental frequency	f^*
F3	Spectral amplitude corresponding to mean frequency	$S\left(\overline{f}\right)$
F4	Spectral amplitude corresponding to fundamental frequency	$S(f^*)$
F5	Phase angle corresponding to mean frequency	$\phi\left(\overline{f}\right)$
F6	Phase angle corresponding to fundamental frequency	$\phi(f^*)$
F7	Average signal energy	$E_a = \sqrt{\frac{1}{n}\sum_{i=1}^{n}\lvert S(f_i)\rvert^2}$

Table 2. *Cont.*

Feature Type Identifier	Name of Feature	Feature Definition
F8	Crest factor	$CF = \frac{S(f^*)}{E_a}$
F9	Spectral crest factor	$SCF = \frac{S(f^*)}{S\left(\overline{f}\right)}$
F10	Relative energy in the first frequency band	$E_{b1} = \frac{\int_0^{B_f} S(f)df}{\int_0^{f_n} S(f)df}$
F11	Relative energy in the second frequency band	$E_{b2} = \frac{\int_{B_f}^{2B_f} S(f)df}{\int_0^{f_n} S(f)df}$
F12	Relative energy in the third frequency band	$E_{b3} = \frac{\int_{2B_f}^{3B_f} S(f)df}{\int_0^{f_n} S(f)df}$
F13	Relative energy in the fourth frequency band	$E_{b4} = \frac{\int_{3B_f}^{4B_f} S(f)df}{\int_0^{f_n} S(f)df}$
F14	Relative energy in the fifth frequency band	$E_{b5} = \frac{\int_{4B_f}^{5B_f} S(f)df}{\int_0^{f_n} S(f)df}$

The identifiers 'T' and 'F' are used to denote time domain features and frequency domain features, respectively.

Table 3. The results of hyperparameter optimization for the models.

Model	Name of Hyperparameter	Searching Range	Optimal Hyperparameter
LightGBM	Boosting type	"GBDT", "Dart", "Goss"	GBDT
	Learning_rate	0.0001, 0.001, 0.01	0.01
	Num_leaves	$2, 2^2, \ldots, 2^{10}$	2^6
	Max_depth	1, 2, . . ., 10	8
	Feature_fraction	0.05, 0.1, . . ., 1	0.35
	Bagging_fraction	0.05, 0.1, . . ., 1	0.25
	N_estimator	100, 150, . . ., 1500	450
KNN	K value	2, 3, . . ., 50	7
	Distance indicator	"chebyshev", "euclidean", "manhattan", "minkowski"	"manhattan"
SVM	C value	1, 10, 100, 1000	100
	Kernel function	"linear", "rbf", "sigmoid"	"rbf"
FNN	Number of hidden units in the first layer	$2^6, 2^7, 2^8, 2^9$	2^8
	Number of hidden units in the second layer	$2^5, 2^6, 2^7$	2^6

On the basis of parameter optimization, further steps of feature selection were carried out. Since extracting a single statistical feature using sliding windows generated multiple feature points, feature selection helped reduce the feature dimensions, decreased the number of features, and improved the computational efficiency of the model. During the feature selection process, the ReliefF method was employed, which is an effective technique for assessing feature importance. The samples used for feature selection still came from the C1 dataset. The ranking results are presented in Table 4. A lower ranking in the importance order indicates a more crucial feature. Due to significant differences in the descriptive aspects of the time domain and frequency domain features, independent rankings were performed for these two feature types during the importance sorting process.

Table 4. Importance ranking of time domain and frequency domain features.

Ranking	Time Domain Indicator	Frequency Domain Indicator
1	T6	F8
2	T7	F7
3	T8	F6
4	T9	F4
5	T4	F9
6	T5	F2
7	T1	F3
8	T10	F10
9	T3	F5
10	T2	F11
11	T11	F1
12	-	F14
13	-	F13
14	-	F12

Building upon the feature representation ranking using the ReliefF method, we further combined LightGBM, k-NN, SVM, and FNN to eliminate redundant features for collision classification in the C1 dataset. Specifically, we followed the importance ranking of the features and sequentially removed less significant time domain and frequency domain features. The removal alternated between time domain and frequency domain features, starting with the removal of frequency domain features. To assess the effectiveness of feature selection, we first shuffled the C1 dataset and then evaluated the selected features using a five-fold cross-validation approach. The classification models used the hyperparameters in Table 3. The final evaluation results are presented in Figure 5. The figure displays the average classification accuracy values of the classification models after removing different features. A higher accuracy indicates a smaller impact on the classification results when the corresponding features are removed. It can be observed that when the total number of retained features was greater than 14, the removed features had little impact on the classification effect. However, as the features were removed, the classification accuracy began to decrease significantly. When the total number of features was 10, compared to the process without feature removal, the classification accuracy dropped by 9.56%. To ensure the effectiveness of the training of the collision classification model while minimizing the number of features, this study utilized a set of 14 selected features in the subsequent experiments. Specifically, these features consisted of the first six time domain features (T6, T7, . . ., T5 in Table 4) and the first eight frequency domain features (F8, F7, . . ., F10 in Table 4).

In the context of collision processing problems, the sequence lengths of collision signals significantly determine the richness of the information embedded in the signals. The appropriate sequence length is crucial because sequences that are too short may lead to insufficient feature information, severely impacting classification performance. Conversely, excessively long sequences may decrease computational efficiency and make the classification method more reliant on sustained collision information post-collision. To determine the suitable information sequence length, we employed a multimodel fusion approach to evaluate the sequence information, using LightGBM and comparison methods. The dataset used for the evaluation was from the C1 dataset, and the feature representation was based on the feature selection results in Table 4. Additionally, the effective period was set from 50 sample points to 350 sample points, with testing conducted at intervals of 30 sample points. The collision classification accuracy results with different effective periods are illustrated in Figure 6. It was seen that as the effective period length increased, the collision classification accuracy of the different classifiers showed an upward trend. When the effective period length reached 290 sample points, further increasing the sequence length resulted in minimal fluctuations in classification accuracy. For the FNN method, there was a decline in classification accuracy. This suggests that when the effective period length reached 290 sample points, the information content was sufficiently rich. Therefore, for subsequent analyses, we set the effective period length of the collision vibration signal to 290 sample points.

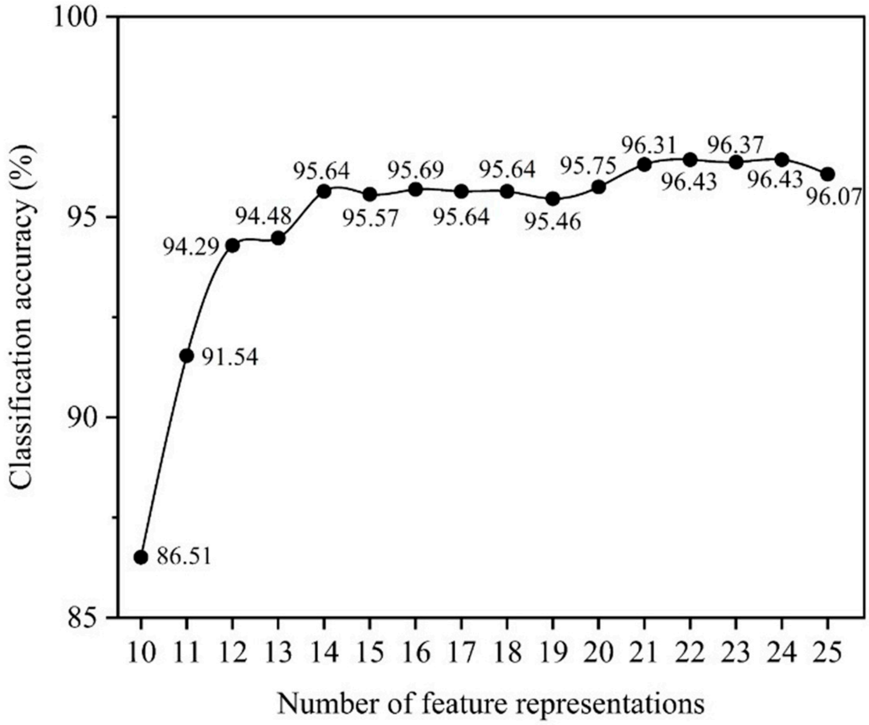

Figure 5. The average collision classification accuracy values of different classification models with varying feature representation quantities.

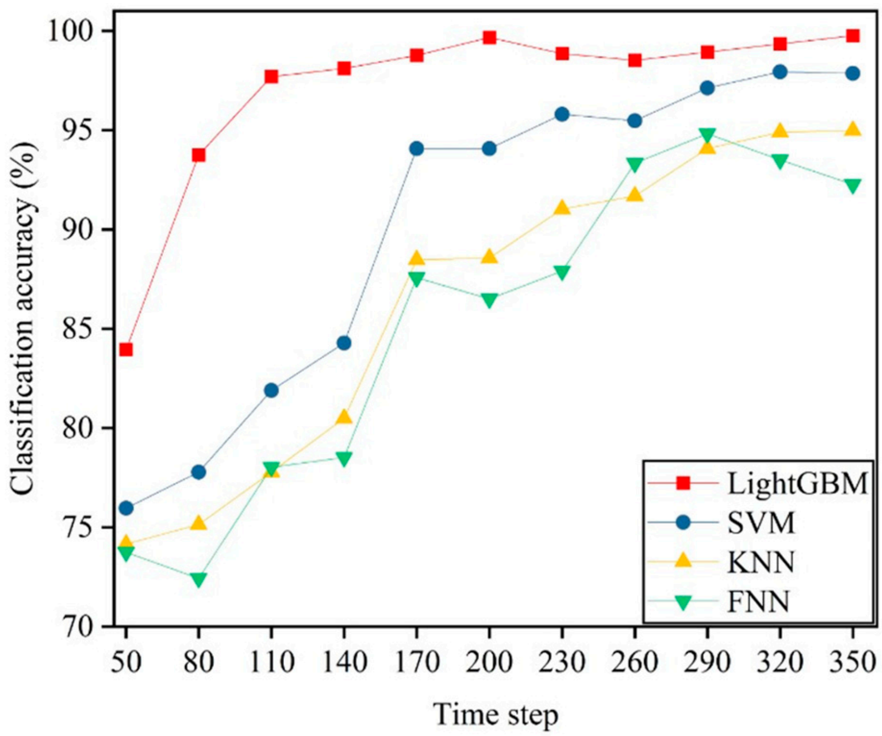

Figure 6. Collision classification accuracy of different models with different effective periods.

4.2. Signal Reconstruction Results

To provide a detailed exposition of the rational implementation of EMD and reconstruction, we selected a segment of a typical x-axis collision vibration signal. Initially, noise was added to the signal with the SNR set to −9 dB. Then, the signal underwent normalization. Finally, the normalized signal underwent the EMD process, resulting in different-order IMF components, as depicted in Figure 7. It is visually evident that the noise details were more pronounced in the first- and second-order IMFs. To mitigate the noise components in a reconstructed signal, one can choose to exclude IMFs containing rich noise details. However, it is essential to note that such IMFs also encompass other valuable signal feature information. Therefore, caution must be exercised during exclusion to prevent excessive removal, which could lead to the loss of features related to the original signal during the reconstruction process.

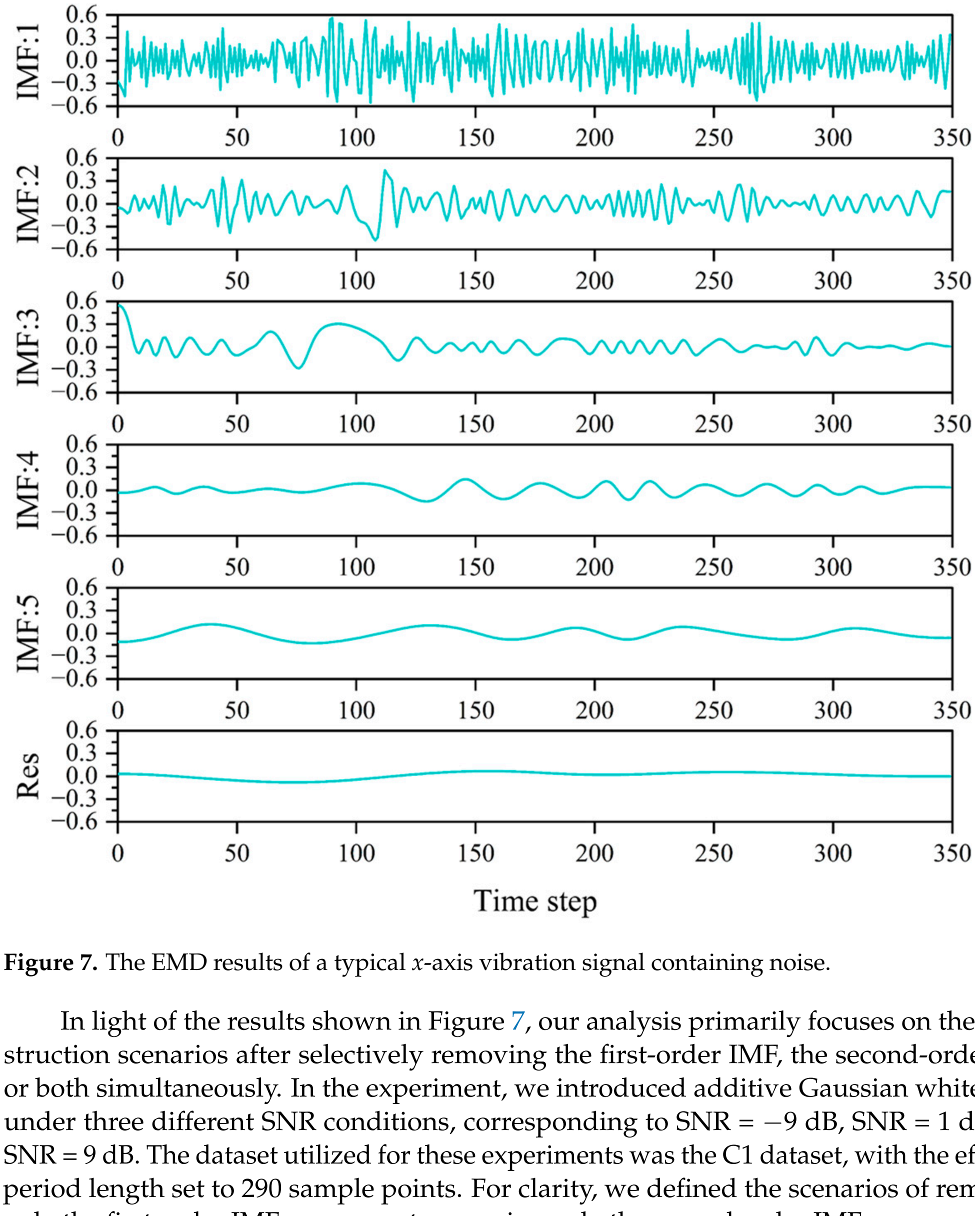

Figure 7. The EMD results of a typical x-axis vibration signal containing noise.

In light of the results shown in Figure 7, our analysis primarily focuses on the reconstruction scenarios after selectively removing the first-order IMF, the second-order IMF, or both simultaneously. In the experiment, we introduced additive Gaussian white noise under three different SNR conditions, corresponding to SNR = −9 dB, SNR = 1 dB, and SNR = 9 dB. The dataset utilized for these experiments was the C1 dataset, with the effective period length set to 290 sample points. For clarity, we defined the scenarios of removing only the first-order IMF component, removing only the second-order IMF component and removing both the first- and second-order IMF components as Case 1, Case 2, and Case 3, respectively. Finally, we evaluated the effectiveness of different removal strategies based on the classification accuracy results. The detailed classification results are illustrated in Figure 8. It is evident that signal reconstruction by solely removing the first-order IMF outperformed scenarios where only the second-order IMF was removed or where both the first- and second-order IMFs were removed simultaneously in terms of the classification results. While this difference was less pronounced at lower noise intensities, as the noise intensity increased, the advantage of solely removing the first-order IMF became significantly more prominent. This finding indicates that in the context of collision classification, for noise suppression, removing only the first-order IMF is more effective in minimizing the loss of valid features in the data compared to other IMF removal strategies. Therefore, it can be considered more reasonable to reconstruct a signal by selectively removing only the first-order IMF component.

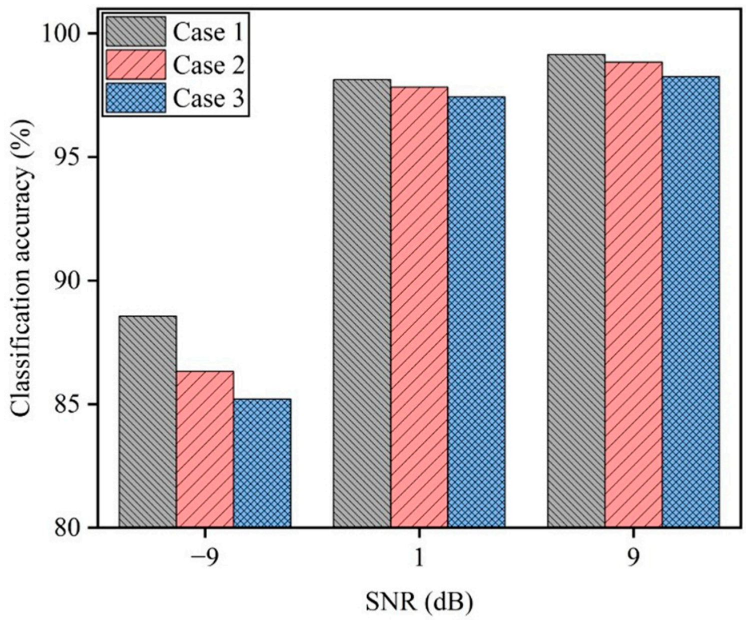

Figure 8. The collision classification accuracy under the exclusion of different IMF components.

4.3. Collision Classification Results under Different Conditions

Furthermore, we conducted an in-depth analysis of collision classification in scenarios where there was no relative deflection angle between the charger and the charging port. To observe the influence of different joint configurations on the results and mitigate potential information leakage issues, we designated the C1 dataset as the training set, while the C2 and C3 datasets served as the test sets. In the experiment, for a detailed examination of the impact of noise on classification results, we introduced noise signals with varying SNRs, ranging from −9 dB to 9 dB, with intervals of 2 dB. Through this experimental design, we gained comprehensive insights into the effect of noise intensity on collision classification performance. Furthermore, we conducted an analysis of the impact of introducing EMD and reconstruction on noise suppression. For comparison, we also employed collision classification methods without the EMD process in the experiment. The average collision classification accuracy results are illustrated in Figure 9.

It can be observed that, as the noise intensity decreased, the classification accuracy of various methods showed a gradual upward trend. In the comprehensive comparison, EMD-LightGBM stood out among the different noise levels, exhibiting a higher overall classification accuracy compared to the other methods. Its maximum average classification accuracy reached an impressive 97.3%. In comparison to the LightGBM method without the introduction of the EMD process, incorporating EMD significantly enhanced the advantage of the collision classification method, particularly in the presence of stronger noise, resulting in a maximum accuracy improvement of up to 3.64%. However, it is noteworthy that among the other classifiers, the introduction of the EMD process did not result in a significant advantage in handling noisy signals. This phenomenon indicates, to some extent, that these classifiers exhibited poor adaptability to signal features after undergoing EMD processing.

Taking all factors into consideration, we believe that in the practical noise suppression process, apart from using EMD combined with reconstruction for noise suppression, the choice of a suitable classifier is also crucial.

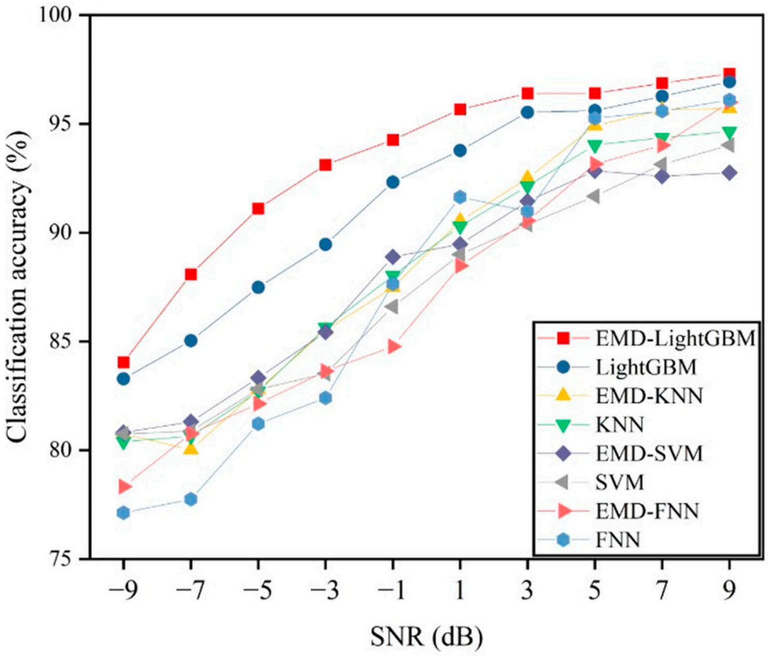

Figure 9. The average collision classification accuracy results with varying levels of noise.

The results in Figure 10 display the collision classification accuracy values of various collision classification methods with the inclusion of the EMD step with different joint configurations. It can be observed that in the case of collisions with no relative angular bias between the charger and the charging port, overall, the accuracy with C2 as the test set was higher than that with C3 as the test set. This phenomenon indicates that the joint configuration had a certain impact on the accuracy results, and when there was significant variation in the joint configuration, the final classification accuracy was lower. The classification accuracy differences between C1 and C2 using different methods were as follows: the maximum accuracy difference for EMD-LightGBM was 0.61%; EMD-KNN's maximum accuracy difference was 0.56%; EMD-SVM's maximum accuracy difference was 0.7%; and EMD-FNN's maximum accuracy difference was 0.52%. Through a comprehensive analysis of these data, we can conclude that although there was an overall trend suggesting that changes in joint configurations had an impact on the collision classification results, this impact did not lead to a significant performance decline. Within the scope of our study, the fluctuation in classification accuracy caused by changes in joint configurations was relatively mild, and it did not trigger significant instability.

To assess the collision classification performance of the proposed method in the presence of relative angular displacement between the charger and the charging port, we employed C1 as the training set and selected datasets with relative angular deviations of 1°, 2°, and 3° (C4, C5, and C6 as the test sets). For a comparative analysis, we also tested SVM, KNN, FNN, and the fusion of these three models with EMD. Figure 11 illustrates the collision classification results with varying levels of noise and different relative angular displacements. Similar to the scenarios without relative angular displacement, as the noise level increased, the collision classification accuracy of all methods notably decreased. Across various noise levels, EMD-LightGBM and LightGBM consistently demonstrated higher average collision classification accuracy compared to the other methods. Their respective highest prediction accuracies reached 91.66% and 90.09%. In scenarios with low noise levels, the presence of relative angular displacement led to significantly lower collision classification accuracy for all methods compared to the scenarios without relative angular displacement. For instance, at SNR=9, the maximum collision classification accuracies for EMD-LightGBM, EMD-SVM, EMD-KNN, and EMD-FNN were 91.66%, 86.04%, 86.46%, and 85.05%, respectively. In comparison to the scenarios without relative angular displacement, these four methods experienced reductions of 5.87%, 6.72%, 8.85%, and 11%, respectively. However, this performance gap diminished noticeably in conditions with more noise. This indicates that the presence of relative angular displacement influenced collision classification, with its impact being more pronounced in conditions with less noise. As noise increased, obscuring the original features of the signal, the influence of relative angular displacement on prediction confusion diminished. Moreover, as the relative angular displacement increased, EMD-LightGBM and EMD-KNN exhibited a declining trend in collision classification accuracy with low noise levels. Therefore, for both of these methods, enhancing the predictive performance of collision classification can be achieved by collecting a more extensive dataset that includes a diverse range of relative angular displacements. It is worth noting that introducing EMD for noise reduction is not universally effective across different methods. For instance, EMD-FNN demonstrated significantly lower collision classification accuracy in high-intensity noise scenarios compared to using FNN alone. This indicates that when the introduction of EMD results in significant changes to features, the classification model needs to exhibit good adaptability to such features to achieve effective noise suppression through integration with EMD.

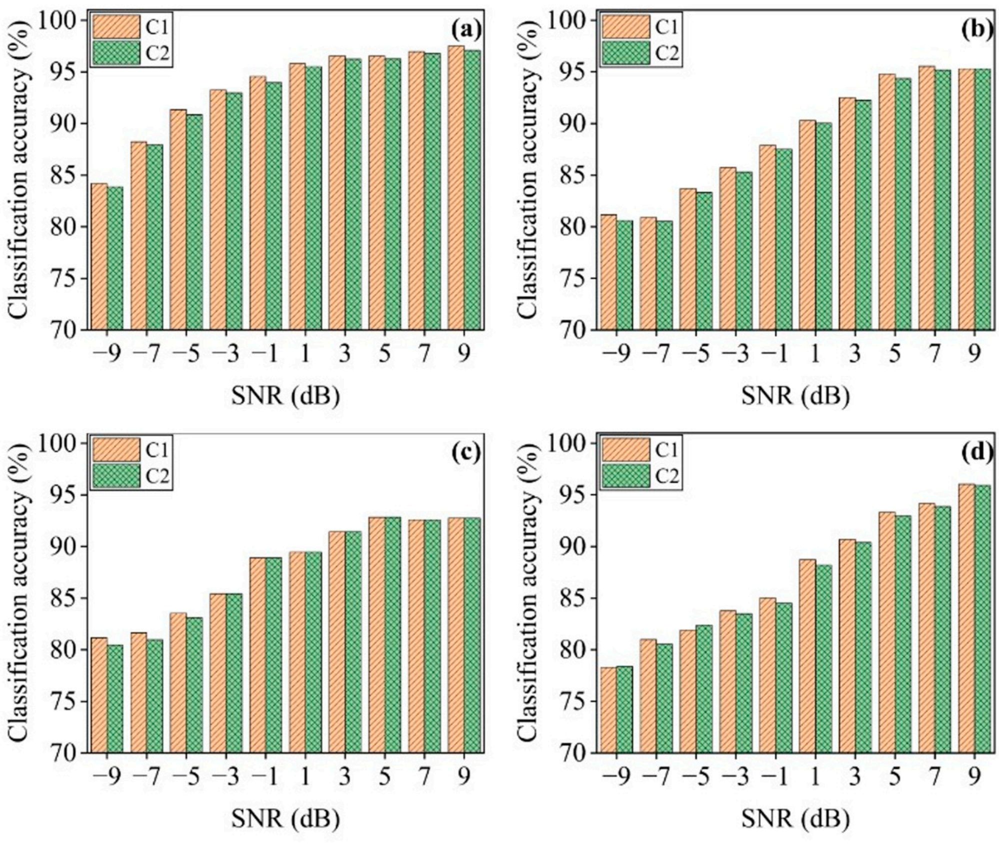

Figure 10. Comparison of collision classification accuracy on C2 and C3 test sets: (**a**) EMD-LightGBM, (**b**) EMD-KNN, (**c**) EMD-SVM, (**d**) EMD-FNN.

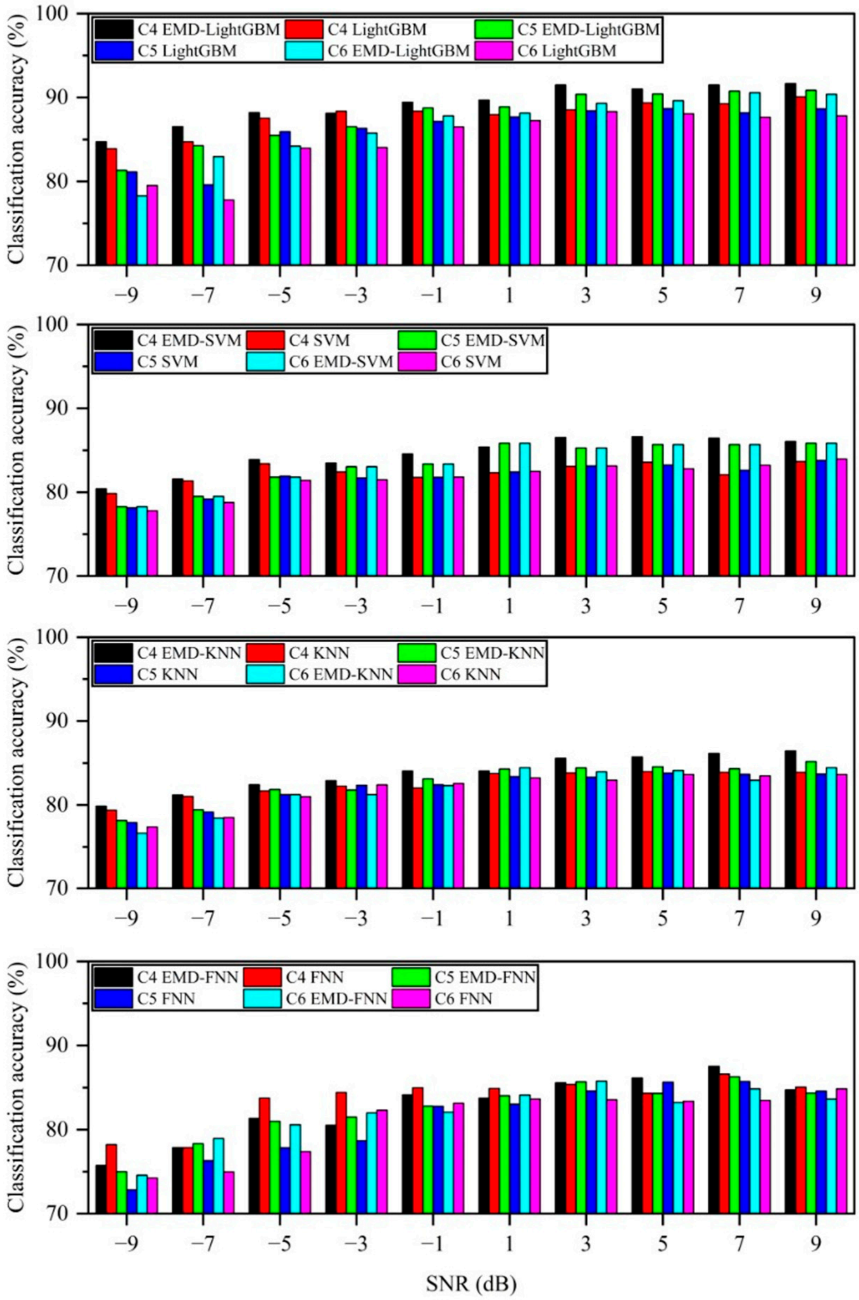

Figure 11. Collision classification accuracy of 8 methods with different noise levels and angular deviations.

5. Conclusions

In this study, we proposed a collision classification scheme tailored for robot manipulators in noisy environments, leveraging EMD and LightGBM. During the data collection phase, a collision point template was meticulously designed to conduct experiments, covering diverse robot execution conditions and ensuring the generation of a representative dataset. After the normalization of the collision vibration signals, feature extraction and selection were performed by analyzing their importance, with multiple models effectively filtering redundant features. Subsequently, the selected features were employed in the analysis of IMFs obtained through EMD. The rationalization of removing IMFs with high noise contents and the subsequent reconstruction of the remaining components formed the basis for training the classification model. The proposed collision classification method demonstrated outstanding predictive capability, surpassing advanced methods reliant on manual feature extraction. Notably, it exhibited superior stability and adaptability to noisy scenarios.

This research significantly bridges a gap in the collision classification domain, specifically for the end effectors of electric vehicle charging robots in noisy environments, thereby contributing to an enhancement in system safety in the automatic charging process. The insights gained from this study pave the way for further advancements in collision processing methodologies. Future research can explore the development of adaptive post-collision response systems, contributing to the establishment of a more comprehensive collision processing system suitable for real-world scenarios in automatic electric vehicle charging applications.

Author Contributions: H.L. developed the methodology; H.L. and P.Q. conceived and designed the experiment; Z.L. conducted the data curation and collection; H.L. wrote the original draft of the paper; S.D. and D.W. reviewed and edited the paper. All authors have read and agreed to the published version of the manuscript.

Funding: This research received no external funding.

Institutional Review Board Statement: Not applicable.

Informed Consent Statement: Not applicable.

Data Availability Statement: The original contributions presented in the study are included in the article, further inquiries can be directed to the corresponding author.

Conflicts of Interest: The authors declare no conflicts of interest.

References

1. Behl, M.; DuBro, J.; Flynt, T.; Hameed, I.; Lang, G.; Park, F. Autonomous Electric Vehicle Charging System. In Proceedings of the 2019 Systems and Information Engineering Design Symposium (SIEDS), Charlottesville, VA, USA, 26 April 2019; IEEE: Charlottesville, VA, USA, 2019; pp. 1–6.
2. Asha Rani, G.S.; Lal Priya, P.S. Design of Automatic Charging System for Electric Vehicles Using Rigid-Flexible Manipulator. In Proceedings of the 2022 Second International Conference on Power, Control and Computing Technologies (ICPC2T), Raipur, India, 1–3 March 2022; IEEE: Raipur, India, 2022; pp. 1–6.
3. Quan, P.; Lou, Y.; Lin, H.; Liang, Z.; Wei, D.; Di, S. Research on Identification and Location of Charging Ports of Multiple Electric Vehicles Based on SFLDLC-CBAM-YOLOV7-Tinp-CTMA. *Electronics* **2023**, *12*, 1855. [CrossRef]
4. Quan, P.; Lou, Y.; Lin, H.; Liang, Z.; Di, S. Research on Fast Identification and Location of Contour Features of Electric Vehicle Charging Port in Complex Scenes. *IEEE Access* **2022**, *10*, 26702–26714. [CrossRef]
5. Quan, P.; Lou, Y.; Lin, H.; Liang, Z.; Wei, D.; Di, S. Research on Fast Recognition and Localization of an Electric Vehicle Charging Port Based on a Cluster Template Matching Algorithm. *Sensors* **2022**, *22*, 3599. [CrossRef] [PubMed]
6. Pan, M.; Sun, C.; Liu, J.; Wang, Y. Automatic Recognition and Location System for Electric Vehicle Charging Port in Complex Environment. *IET Image Process* **2020**, *14*, 2263–2272. [CrossRef]
7. Sun, C.; Pan, M.; Wang, Y.; Liu, J.; Huang, H.; Sun, L. Method for Electric Vehicle Charging Port Recognition in Complicated Environment Based on CNN. In Proceedings of the 2018 15th International Conference on Control, Automation, Robotics and Vision (ICARCV), Singapore, 18–21 November 2018; IEEE: Singapore, 2018; pp. 597–602.
8. Zhang, Z.; Qian, K.; Schuller, B.W.; Wollherr, D. An Online Robot Collision Detection and Identification Scheme by Supervised Learning and Bayesian Decision Theory. *IEEE Trans. Automat. Sci. Eng.* **2021**, *18*, 1144–1156. [CrossRef]
9. Haddadin, S.; De Luca, A.; Albu-Schaffer, A. Robot Collisions: A Survey on Detection, Isolation, and Identification. *IEEE Trans. Robot.* **2017**, *33*, 1292–1312. [CrossRef]
10. de Luca, A.; Mattone, R. Sensorless Robot Collision Detection and Hybrid Force/Motion Control. In Proceedings of the 2005 IEEE International Conference on Robotics and Automation, Barcelona, Spain, 18–22 April 2005; IEEE: Barcelona, Spain, 2005; pp. 999–1004.
11. Gordić, Z.; Jovanović, K. Collision Detection on Industrial Robots in Repetitive Tasks Using Modified Dynamic Time Warping. *Robotica* **2020**, *38*, 1717–1736. [CrossRef]
12. Vorndamme, J.; Schappler, M.; Haddadin, S. Collision Detection, Isolation and Identification for Humanoids. In Proceedings of the 2017 IEEE International Conference on Robotics and Automation (ICRA), Singapore, 29 May–3 June 2017; IEEE: Singapore, 2017; pp. 4754–4761.
13. Li, X.; Zhang, Y.; Xie, X.; Li, J.; Shi, G. Improving Robotic Tactile Localization Super-Resolution via Spatiotemporal Continuity Learning and Overlapping Air Chambers. *AAAI* **2023**, *37*, 6192–6199. [CrossRef]

14. Min, F.; Wang, G.; Liu, N. Collision Detection and Identification on Robot Manipulators Based on Vibration Analysis. *Sensors* **2019**, *19*, 1080. [CrossRef]
15. Lin, H.; Quan, P.; Liang, Z.; Lou, Y.; Wei, D.; Di, S. Collision Localization and Classification on the End-Effector of a Cable-Driven Manipulator Applied to EV Auto-Charging Based on DCNN–SVM. *Sensors* **2022**, *22*, 3439. [CrossRef]
16. Popov, D.; Klimchik, A.; Mavridis, N. Collision Detection, Localization & Classification for Industrial Robots with Joint Torque Sensors. In Proceedings of the 2017 26th IEEE International Symposium on Robot and Human Interactive Communication (RO-MAN), Lisbon, Portugal, 28 August–1 September 2017; IEEE: Lisbon, Portugal, 2017; pp. 838–843.
17. De Luca, A.; Albu-Schaffer, A.; Haddadin, S.; Hirzinger, G. Collision Detection and Safe Reaction with the DLR-III Lightweight Manipulator Arm. In Proceedings of the 2006 IEEE/RSJ International Conference on Intelligent Robots and Systems, Beijing, China, 9–15 October 2006; IEEE: Beijing, China, 2006; pp. 1623–1630.
18. Lippi, M.; Gillini, G.; Marino, A.; Arrichiello, F. A Data-Driven Approach for Contact Detection, Classification and Reaction in Physical Human-Robot Collaboration. In Proceedings of the 2021 IEEE International Conference on Robotics and Automation (ICRA), Xi'an, China, 30 May–5 June 2021; IEEE: Xi'an, China, 2021; pp. 3597–3603.
19. Del Prete, A.; Nori, F.; Metta, G.; Natale, L. Control of Contact Forces: The Role of Tactile Feedback for Contact Localization. In Proceedings of the 2012 IEEE/RSJ International Conference on Intelligent Robots and Systems, Vilamoura-Algarve, Portugal, 7–12 October 2012; IEEE: Vilamoura-Algarve, Portugal, 2012; pp. 4048–4053.
20. Kalafat, M.A.; Yildiz, A.F. Development of a Soft Tactile Sensor Array for Contact Localization Estimations. *IEEE Access* **2022**, *10*, 112053–112065. [CrossRef]
21. McMahan, W.; Romano, J.M.; Kuchenbecker, K.J. Using Accelerometers to Localize Tactile Contact Events on a Robot Arm. In Proceedings of the Workshop on Advances in Tactile Sensing and Touch-Based Human-Robot Interaction, ACM/IEEE International Conference on Human-Robot Interaction, Boston, MA, USA, 5–8 March 2012.
22. Dev Anand, M.; Selvaraj, T.; Kumanan, S. Fault Detection and Fault Tolerance Methods for Industrial Robot Manipulators Based on Hybrid Intelligent Approach. *Adv. Produc. Engineer. Manag.* **2012**, *7*, 225–236. [CrossRef]
23. Milecki, A.; Nowak, P. Review of Fault-Tolerant Control Systems Used in Robotic Manipulators. *Appl. Sci.* **2023**, *13*, 2675. [CrossRef]
24. Lecun, Y.; Bottou, L.; Bengio, Y.; Haffner, P. Gradient-Based Learning Applied to Document Recognition. *Proc. IEEE* **1998**, *86*, 2278–2324. [CrossRef]
25. Elman, J.L. Finding Structure in Time. *Cogn. Sci.* **1990**, *14*, 179–211. [CrossRef]
26. Iyer, A.; Das, S.S.; Teotia, R.; Maheshwari, S.; Sharma, R.R. CNN and LSTM Based Ensemble Learning for Human Emotion Recognition Using EEG Recordings. *Multimed. Tools Appl.* **2023**, *82*, 4883–4896. [CrossRef]
27. Arun Prasath, G.; Annapurani Panaiyappan, K. Design of an Integrated Learning Approach to Assist Real-Time Deaf Application Using Voice Recognition System. *Comput. Electr. Eng.* **2022**, *102*, 108145. [CrossRef]
28. Aljemely, A.H.; Xuan, J.; Al-Azzawi, O.; Jawad, F.K.J. Intelligent Fault Diagnosis of Rolling Bearings Based on LSTM with Large Margin Nearest Neighbor Algorithm. *Neural Comput. Appl.* **2022**, *34*, 19401–19421. [CrossRef]
29. An, Y.; Zhang, K.; Liu, Q.; Chai, Y.; Huang, X. Rolling Bearing Fault Diagnosis Method Base on Periodic Sparse Attention and LSTM. *IEEE Sensors J.* **2022**, *22*, 12044–12053. [CrossRef]
30. Lin, H.; Lou, Y.; Quan, P.; Liang, Z.; Wei, D.; Di, S. Small-Scale Zero-Shot Collision Localization for Robots Using RL-CNN. *Appl. Sci.* **2023**, *13*, 4079. [CrossRef]
31. Ke, G.; Meng, Q.; Finley, T.; Wang, T.; Chen, W.; Ma, W.; Ye, Q.; Liu, T.-Y. LightGBM: A Highly Efficient Gradient Boosting Decision Tree. In Proceedings of the Advances in Neural Information Processing Systems, Long Beach, CA, USA, 4–9 December 2017.
32. Sun, X.; Liu, M.; Sima, Z. A Novel Cryptocurrency Price Trend Forecasting Model Based on LightGBM. *Financ. Res. Lett.* **2020**, *32*, 101084. [CrossRef]
33. Huang, N.E.; Shen, Z.; Long, S.R.; Wu, M.C.; Shih, H.H.; Zheng, Q.; Yen, N.-C.; Tung, C.C.; Liu, H.H. The Empirical Mode Decomposition and the Hilbert Spectrum for Nonlinear and Non-Stationary Time Series Analysis. *Proc. R. Soc. Lond. A* **1998**, *454*, 903–995. [CrossRef]
34. Kononenko, I. Estimating Attributes: Analysis and Extensions of RELIEF. In *Machine Learning: ECML-94*; Bergadano, F., Raedt, L., Eds.; Lecture Notes in Computer Science; Springer: Berlin/Heidelberg, Germany, 1994; Volume 784, pp. 171–182. ISBN 978-3-540-57868-0.
35. Shekar, B.H.; Dagnew, G. Grid Search-Based Hyperparameter Tuning and Classification of Microarray Cancer Data. In Proceedings of the 2019 Second International Conference on Advanced Computational and Communication Paradigms (ICACCP), Gangtok, India, 25–28 February 2019; IEEE: Gangtok, India, 2019; pp. 1–8.